Lab on a Chip

PAPER

View Article Online
View Journal | View Issue



Cite this: *Lab Chip*, 2025, **25**, 2182

# Ignition of non-equilibrium methane dielectric barrier discharges in a multiphase plasma–liquid microfluidic device†

Sudip Das,[a] Mackenzie Meyer,[b] Mark J. Kushner[b] and Ryan L. Hartman *[a]

Received 24th January 2025,
Accepted 5th March 2025

DOI: 10.1039/d5lc00090d

rsc.li/loc

Atmospheric pressure plasma conversion of methane is usually addressed in gas-only systems, such as dry reforming of methane. Introducing a liquid in such a system enables direct utilization of plasma-produced radicals, such as methyl ($CH_3$), as a reactant in the liquid. Methylation of organic liquids by this technique can lead to the sustainable production of high-value products. A dielectric-barrier-discharge (DBD) microfluidic reactor having a 500 μm × 500 μm cross-section was developed to investigate the characteristics of methane-containing atmospheric pressure plasmas in contact with organic solvents. The sensors included optical emission spectroscopy and chip surface temperature measurement to estimate and predict plasma initiation in these methane-containing systems and provide insights into the plasma–liquid interfacial behavior. Fluids having high liquid hold-up, low boiling point, and low dielectric constant have been found to have adverse effects on non-equilibrium DBD methane plasma ignition.



## Introduction

Carbon utilization to reduce the emission of greenhouse gases (GHGs) is the focus of multidisciplinary research. The production of methane ($CH_4$), the primary component of natural gas (~95%, volume basis),[1] was 2.92 billion cubic meters per day in 2020, totaling around 1.06 trillion cubic meters for the year.[2] The vast majority of this methane was used for combustion and feedstock material for the chemical industry. A significant fraction of this methane was flared as a by-product of oil extraction, resulting in the emission of $CO_2$, bypass $CH_4$, and combustion products such as $NO_x$. Locally capturing and converting this otherwise wasted methane to higher-value products would reduce the emission of GHGs, provide financial benefit, and possibly offset the use of liquid fuels as feedstocks.

Methane conversion is challenging because of the high C–H bond dissociation energy (~439 kJ $mol^{-1}$ or ~4.55 eV per atom)[3] and the resulting difficulty in activating $CH_4$ (activation refers to the production of $CH_x$ radicals that can participate in additional reactions). The energy-intensive process of thermal cracking, which requires temperatures between 1200 °C and 1600 °C at 1 atm, is typically used to convert methane into higher-order hydrocarbons such as butadiene, benzene, and toluene.[4] This process has limited selectivity of the desired products. An alternate activation process is C–H bond cleavage through electron impact processes in non-thermal plasmas. Several experimental and computational investigations of $CH_4$ conversion in non-equilibrium low-temperature plasmas have been conducted, with and without a catalyst (or the dielectric support).[5] Typically, the dominant products are syngas components ($CO/H_2$).[6] The direct production of gaseous oxygenates[7] and higher hydrocarbons have also been investigated,[8] as have the direct conversion to liquids, which typically has a small rate of production.[9] Plasma-based conversion of $CH_4$ is sensitive to the choice of gas mixture, catalyst, and excitation method (*e.g.*, microwave *vs.* pulsed discharge), which emphasizes the need for a system approach in selecting the optimal operating conditions for directly converting $CO_2$ and $CH_4$ into value-added oxygenates with higher selectivity. For example, plasma catalysis in a dielectric barrier discharge (DBD) was reported by Yi *et al.*, *i.e.* for $NH_3$ reforming of $CH_4$ over Cu-based catalysts, producing HCN and $H_2$ at a reduced temperature,[10] and for the selective oxidation of $CH_4$ to $CH_3OH$.[11]

Plasma chemical conversion of methane has been extensively investigated in DBDs,[12] with and without catalyst loading. The electron temperature in DBDs is typically several eV while the gas temperature remains near ambient. The low gas temperature potentially enables high selectivity of the conversion process as non-selective endothermic reactions are minimized. The high electron temperature enables

[a] *Department of Chemical and Biomolecular Engineering, New York University, NY 11201, USA. E-mail: ryan.hartman@nyu.edu*
[b] *Department of Electrical and Computer Engineering, University of Michigan, MI 48109, USA*

† Electronic supplementary information (ESI) available. See DOI: https://doi.org/10.1039/d5lc00090d

efficient electron impact dissociation and ionization of methane (activation) initially producing $CH_3$, $CH_2$, H, and $CH_4^+$. In mixtures of $CH_4$ with rare gases, excitation and ionization of the rare gas leads to dissociative excitation transfer to $CH_4$, Penning ionization and charge exchange produce similar dissociation products and ions of $CH_4$ as direct electron impact. Possible reaction pathways and plasma-induced products are discussed in section S1 of ESI.†

Conventional atmospheric pressure DBDs typically have electrode separations of many mm to a few cm, with the pulsed plasmas often being filamentary. These conditions present challenges in controlling the characteristics of plasma and the conversion process. This is particularly the case for systems that use catalysts in which the transport of plasma-produced radicals to the surface of the catalyst is required. DBDs sustained in microreactors address several of these challenges, as the small dimensions enable efficient heat and mass transfer, safety, and control of operating parameters. The small dimensions also accelerate the transport of plasma-produced radicals to surfaces. This latter property is particularly important given the high reactivity of methyl radicals which, in the absence of intervention, would dominantly recombine to form ethane ($C_2H_6$). The rapid transport of $CH_3$ to surfaces in microreactors provides the opportunity to convert methane into higher-value chemical compounds by reaction of methyl radicals with, for example, a solid catalyst. One variety of microreactor is a microfluidic lab-on-a-chip which then opens the possibility of the surface being a liquid organic compound.

Non-thermal atmospheric pressure plasmas (NTPs) sustained in micro-discharge reactors have been investigated by Patinglag *et al.*,[13] Ishii *et al.*,[14] and Yamanishi *et al.*[15] Patinglag *et al.* utilized a micro-DBD configuration in a borosilicate substrate with channel depths of 50–100 μm and widths of 330–390 μm to produce oxygen, air, and argon plasmas in an annulus surrounded by water (annular flow) to investigate water purification. The sinusoidal peak-to-peak applied voltage was 10 kV at 17 kHz with operating pressures of 1 to 2 atm. Ishii *et al.* utilized a borosilicate microreactor with channel dimensions of 400 μm width by 250 μm deep covered with a top indium tin oxide (ITO) electrode and bottom silver electrode to enable imaging of the plasma. Atmospheric pressure plasmas sustained in mixtures of Ar/$CH_4$/$H_2$ produced by 10 kHz, 5–10 kV (peak-to-peak) power were investigated for the synthesis of diamondoids.

Wengler *et al.*[16] demonstrated the feasibility of plasma–liquid interfacial reactivity in a DBD microreactor. Their goal was to oxidize liquid cyclohexane using oxygen plasma. They were able to form oxygenates and other molecules, such as cyclohexyl hydroperoxide, cyclohexanone, cyclohexanol, and cyclohexene by establishing oxygen plasma–cyclohexane annular flow.

In this paper, we report on the electrical characterization of a DBD–microfluidic system in which methane-containing gas mixtures are in contact with organic liquids. The emphasis is on the initiation of plasma. Liquids with lower boiling points (and higher vapor pressure) and lower dielectric constants impeded plasma formation. The data analysis integrated optical emission spectroscopy with chip surface temperature monitoring to gain deeper insights into the dynamics at the plasma–liquid interface. The chip surface temperature profile was obtained using an infrared (IR) thermal camera. In parallel, optical emission spectroscopy was used to monitor plasma generation. This combined approach was applied to single-phase and multiphase microfluidic systems and enabled the estimation of the plasma ignition threshold.

## Description of the experiment and device

### The chip

**Design philosophy.** General gas–liquid annular flow in microchannels in the absence of plasmas has been extensively investigated. The focus here will be on the studies conducted by Huh *et al.*[17] and Cubaud *et al.*[18] Cubaud *et al.* conducted air–water flow experiments with a microfluidic device constructed from silicon and Borofloat® glass to take advantage of the molecular affinity of the water to silicon. This affinity affects the shape of the meniscus formed in the microchannels. The shape of the meniscus depends on the number of sides of the microchannel ($N$) and the contact angle ($\theta_C$) that the liquid makes at the solid–liquid–gas interface. If $\theta_C < \pi/N$, the flow will be annular, where the gas fills the core/center with the liquid hugging the surfaces. Typically, in gas–liquid flowing systems, the contact angle ($\theta_C$) is proportional to the capillary number ($\theta_C \propto Ca^{1/3}$). Cubaud *et al.* utilized a cross-shaped inlet configuration to mix the gas and the liquid, which they observed produced a steady and homogeneous flow. The square microchannel had widths of 200 μm and 525 μm resulting in bubbles remaining in the center of the channel. For partially wetting microchannels (such as a silicon-glass configuration), five flow regimes are expected depending on the flow rates of the fluids and dimensions of the microchannels: bubbly, wedging, slug, annular, and dry. Flow regime transitions are functions of the gas and liquid superficial velocities. The flow regime transitions occur at specified liquid holdups ($\varepsilon_L$), a parameter for mass transfer correlations in multiphase flows. For a gas–liquid multiphase flow, liquid holdup is the fraction of the liquid relative to the total flow,[19]

$$\varepsilon_L = \frac{Q_L}{Q_L + Q_G} \quad (1)$$

where $Q_L$ and $Q_G$ denote the flow rates of the liquid and the gas phase, respectively.

In annular flow, the film thickness of the liquid is thinner than for wedging and slug flows. The pressure drop for annular flow asymptotically approaches that of single-phase gas flow. The fraction of gas for this flow regime is $\varepsilon_G \geq 0.96$, so the pressure drop would be practically similar to that for $\varepsilon_G = 1$. For single-phase flow, the pressure drop along a microchannel for a given fluid can be calculated using the Hagen-Poiseuille equation. Deriving the pressure drop for

two-phase flow for the specific flow regimes is dependent on the particular gas–liquid system. Cubaud *et al.* used water and air for their system and derived expressions for the fluidic resistance and the pressure drop with respect to water and air based on empirical data. Huh *et al.* suggested that surface forces predominate over other forces (*i.e.*, inertial, gravitational) at the specific flow rates of interest.[17]

The chemical affinity effects imparted by the surface walls, hydrophobicity *vs.* hydrophilicity, are important to characterizing two-phase flow in microchannels. Two dimensionless parameters used to characterize multiphase (gas–liquid) flow are the confinement number (Co) and the Eotvos number (Eo). They describe the ratio between the surface tension forces and the buoyancy forces. Typically, for surface force dominating fluid flow in microchannel, Co $>$ 3.3 (ref. 20) and Eo $>$ 1,[21] can be used to characterize the shape of interfaces between different fluids. The relative magnitude of buoyant forces (gravitational forces and differences in densities between fluids) becomes smaller than surface forces as the dimension of the microchannel decreases. Huh *et al.* reported on seven flow regimes for hydrophobic microchannels and two flow regimes for hydrophilic microchannels. The hydrophobic microchannels (untreated poly-dimethylsiloxane (PDMS)) had a water contact angle of 111°, whereas the hydrophilic microchannels (PDMS treated by plasma oxidation) had a contact angle of 35°. For this work, a microfluidic device (hereafter referred to as μR) was constructed out of silicon and Borofloat® glass.

**Fabrication methodology.** A schematic of μR used in this study is in Fig. 1. The μR was designed based on the transport phenomenon principles discussed by Cubaud *et al.*, Huh *et al.*, Patinglag *et al.*, and Wengler *et al.* In this μR, a separate feedstock mixing zone and a ~1 m long reaction zone were implemented. Lithography for fabrication was accomplished by UV exposure (650 mJ cm$^{-2}$) of photoresist (SPR-220-7) spun at 3000 RPM producing a film thickness of ~7 μm and developed using an MF-26A bath. Deep reactive ion etching (DRIE) of the Si wafer was performed using Oxford Instrument PlasmaPro 100 Cobra inductively coupled plasma using $CF_4$. After 40 minutes of etching, the wafer was cleaved and analyzed with a Filmetrics Inc. microscope. The etch depth was ~270 μm (etch rate of ~6.7 μm min$^{-1}$). Further details of the design and fabrication process are in section S2 of ESI.† A through-chip etch was necessary to create ports that run from the top face of the silicon through to the bottom face of the silicon. This allows fluids to enter from the bottom of the device and flow through the etched microchannels that are confined by silicon and Borofloat® glass. The required time for each fabrication step is listed in Table S1.†

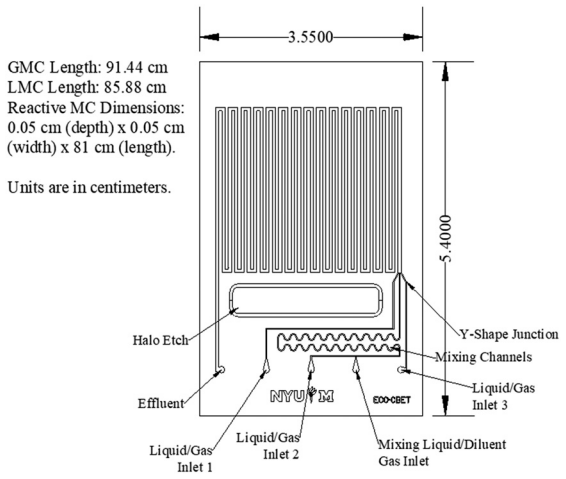


Fig. 1 Schematic diagram (top view) of the μR chip used in this study (MC – microchannel, G – gas, L – liquid).

The μR was fabricated using a silicon wafer and a Borofloat® wafer. Silicon dioxide and indium-tin-oxide (ITO) were deposited to produce electrode contacts. The silicon and the Borofloat® wafers were sourced from Silicon Valley Microelectronics, Inc. The silicon wafers were double-side polished and made of CZ silicon with P/boron dopant, 100 mm in diameter, 1000 μm in thickness, and have a resistivity of 1–50 ohm cm. The Borofloat® wafers were made of Borofloat 33 and were double-sided polished, 100 mm in diameter, and 500 μm in thickness.

## Experimental setup

The experimental setup consists of a fluid delivery system and a plasma generation circuit. Fluid delivery was accomplished using two Teledyne ISCO 2000 series gas pumps, connected to methane and argon gas cylinders. To ensure safety in the gas lines, purge lines were employed using three-way and needle valves. The liquid delivery was performed by Harvard PHD Ultra series syringe pumps equipped with glass Hamilton syringes. To mitigate the possibility of back-flow due to a change of pressure during operation, check valves were employed in both gas and liquid inlet lines before the inlet ports of the μR. The microfluidic lines, tubing, connectors, and in-line blocks were made of polyether ether ketone (PEEK) sourced from Swagelok Technologies Inc. The process flow ends with collecting the samples through the microreactor outlet port. The liquid chemicals (purity >99.5% weight basis, anhydrous, analytical standard grade) were sourced from Merck Inc. and were used as procured. Ultrapure argon and methane gas (UHP grade, >99.99% volume basis) were sourced from AirGas USA LLC.

The plasma was produced using pulsed voltage provided by an Eagle Harbor Inc. Nanosecond pulse generator (model NSP-120-20). The low-impedance NSP generator delivers positive voltage pulses up to 20 kV with an average power of up to 120 W. The maximum pulse repetition frequency (PRF) is 10 kHz with a maximum pulse width of 500 ns. The positive lead of the NSP was connected to the ITO-coated Si-surface (top surface) of the μR chip. A copper tape pasted on the bottom glass layer of the chip was connected to the ground lead of the NSP. Temperature measurements were performed by an ICI infrared (IR) thermal camera (model 9640P, pixel resolution 640 × 480, measurement accuracy:

 

±1 °C). The flow was imaged using a VWR stereo trinocular microscope equipped with a 12-megapixel Moticam S12 microscopic camera. For optical emission spectroscopy (OES) analyses, an Ocean Optics HR4PRO spectrometer (range of wavelength 220–1100 nm) was used. Further details of the experimental setup are in section S3 of the ESI.†

## Methodology

**Plasma-assisted multiphase microfluidics.** Plasma formation in the microchannels was observed by OES and the chip surface temperature was measured by the IR camera (operated using 30 Hz frame rate and 14-bit dynamic range). OES measurements were made in a dark fume hood, with the light-capturing end of an optical fiber (Ocean Optics, UV-vis wavelength range 300–1100 nm, 300 μm core diameter) placed ~1 mm above the central section of the chip top surface. The optical fiber was connected to a spectrometer (optical resolution: FWHM 0.06–7.24 nm). For all experiments, the spectral images were collected for ~45–60 seconds after application of the voltage.

The chip-chuck-clamp assembly and the plasma emission are shown in Fig. 2. Before using the IR camera for experimental data acquisition, it was calibrated by observing hot paraffin oil over the range of 20–80 °C. Before every set of experiments, the performance of the pumps was calibrated. Several solvents were flown through the μR. Once an experiment was completed for one solvent, the microchannels were washed by high throughput pulses of high-purity acetone and/or tetrahydrofuran (THF) using an in-house developed rigorous flooding-drying cycle. Hazards related to the use of high-voltage electrification, corrosive acidic environments, and flammable chemicals (gas and liquid) have been considered and taken care of with extreme sincerity. Detailed step-by-step experimental procedures for plasma–liquid interfacial characterization, subsequent microchannel cleaning, and related safety precautions are discussed in section S4 of ESI.†

**Data analysis.** Plasma OES and IR sensor-based temperature measurements were the primary data used in this investigation. The temperature ($T$) readings were plotted against the applied voltage ($V$). The applied voltage reported herein is per the dial marking on the NSP generator connected to the chip surfaces through low-resistance probes (UL-certified, flame-tested 12-gauge AWM 3239 type, rated for 25 kV DC and 150 °C). Differential voltages across the chip surfaces were measured by a Tektronix THDP0100 model high-voltage differential probe attached to a Tektronix THS3000 series oscilloscope. As shown in section S5 of the ESI,† the accuracy of the output voltage setpoint on the NSP generator was verified by comparing the setpoint values with the measured potential difference. The resulting S-shaped sigmoidal growth trends of chip surface temperature ($T$) with increasing amplitude of applied voltage were then fitted to the experimental $T(V)$ dataset by nonlinear regression using

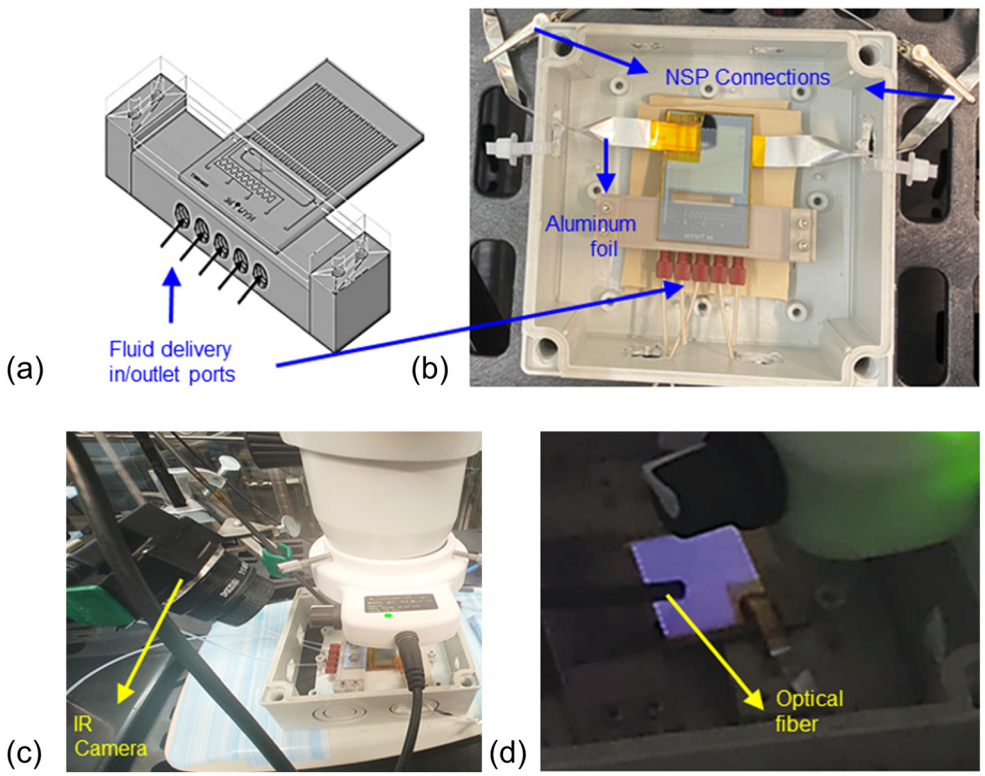


**Fig. 2** Experimental setup. (a) Drawing of the microreactor chip, chuck, and clamp assembly. (b) Image of the microreactor assembly with in/outlet ports. (c) Position of the microreactor about the analytical instruments, *i.e.*, the optical fiber and the IR camera. (d) Position of the optical fiber with plasma glow in the background.

the Levenberg–Marquardt algorithm available as built-in the *DoseResp* function in Origin Pro v8.6.[22]

The abrupt change in chip surface temperature with a small change in operating voltage may be attributed to the formation of plasma in the microchannels and can be inferred as the threshold for plasma ignition. To track the rate of change in measured chip-surface temperature, the fitted $T(V)$ curves with estimated regression parameters were differentiated twice ($d^2T/dV^2$ or $T''(V)$). Three points of interest were the point of rise (corresponding to the maximum value of $T''(V)$), the point of inflection (corresponding to the zero value of $T''(V)$), and the point of saturation (corresponding to the minimum value of $T''(V)$). The OES provided the threshold voltage above which clear plasma spectra could be observed. To check the reliability of this comparative data analysis technique, the points of interest obtained from $T''(V)$ profiles were then compared with the threshold voltage obtained from the OES spectra. This comparison would lead to identifying the threshold voltage amplitude required for plasma ignition in any semi-/non-transparent microreactor chip surface where OES cannot be utilized to investigate plasma formation.

## Results and discussions

### Temperature data acquisition

As indicated in Fig. 3a, the temperature of a circular portion (~5 mm diameter) at the central section of the top surface of the microreactor chip was measured. The sample measured represents a differential slice of a continuous flow reactor initially operated at a steady state. The chip surface temperature reached its quasi-constant value. ~45–60 seconds after switching on the NSP. As shown in Fig. 3b, the average of 4–5 readings taken between 60 s and 180 s was the measured temperature. Values for different experiments are shown. Run 1 and 2 denote the $T(t)$ response for ArMe20 (*i.e.*, 20% volume basis methane in argon) feed gas mixture measured when 200 ns pulses at 10 kHz pulse repetition frequency (PRF) were applied at 6 kV and 7 kV, respectively. The gas flow rate was kept constant at 5 mL $min^{-1}$ for both cases which corresponds to a residence time of ~2.5 seconds. The corresponding thermal images are shown in Fig. 3c and d. Each experiment performed in this study was run in triplicate and the measurement error was ~±2 °C. This error is close to that of the manufacturer-provided measurement uncertainty of the IR-based thermal camera of ±1 °C.

### $T(V)$ analyses

This section contains a discussion on the post-experiment analysis of $T(V)$ data using the $T(V)$ response observed for argon-only (ArMe0) feedstock. The points shown in Fig. 4a are the average temperature of the top surface of the microreactor chip resulting from three sets of experimental measurements. The error bars show ± [maximum absolute error] for each temperature. The solid line shown in Fig. 4a is the regressed fit

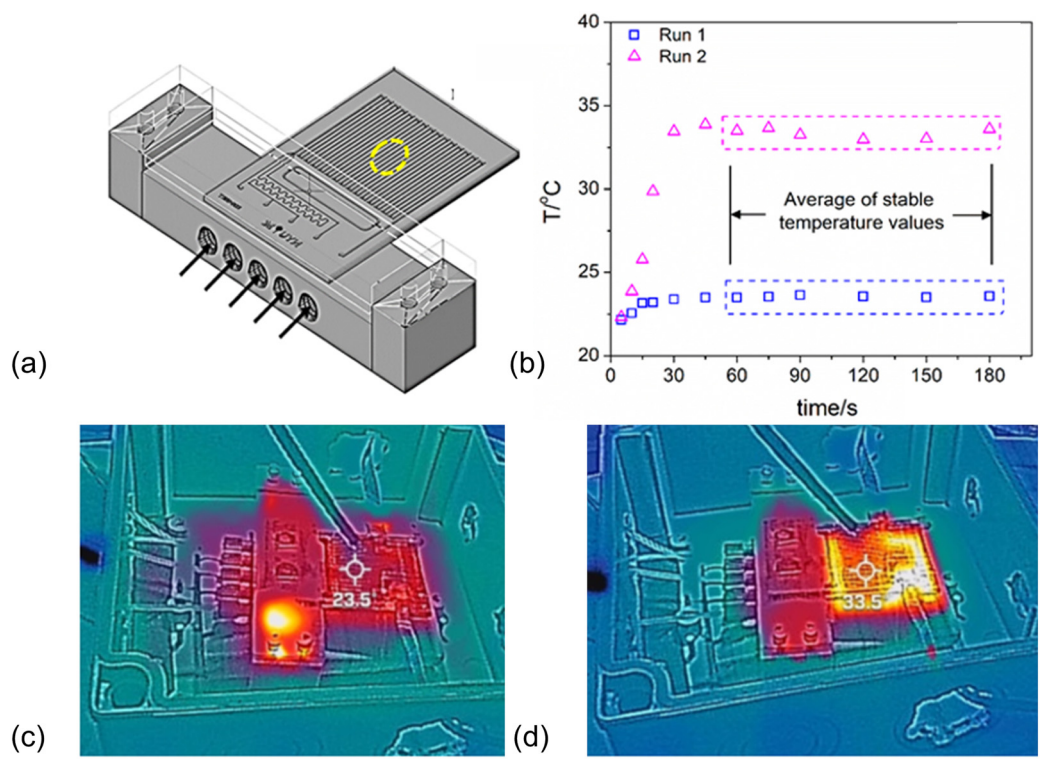


Fig. 3 Details of IR camera-assisted chip surface temperature measurement. (a) The yellow circle marks the section of the chip surface used for temperature measurement. (b) Stabilization of chip surface temperature shown for 2 different runs (marked as run 1 and run 2). (c) and (d) IR-camera generated thermal image of the microreactor chip for run 1 and run 2, respectively.

 

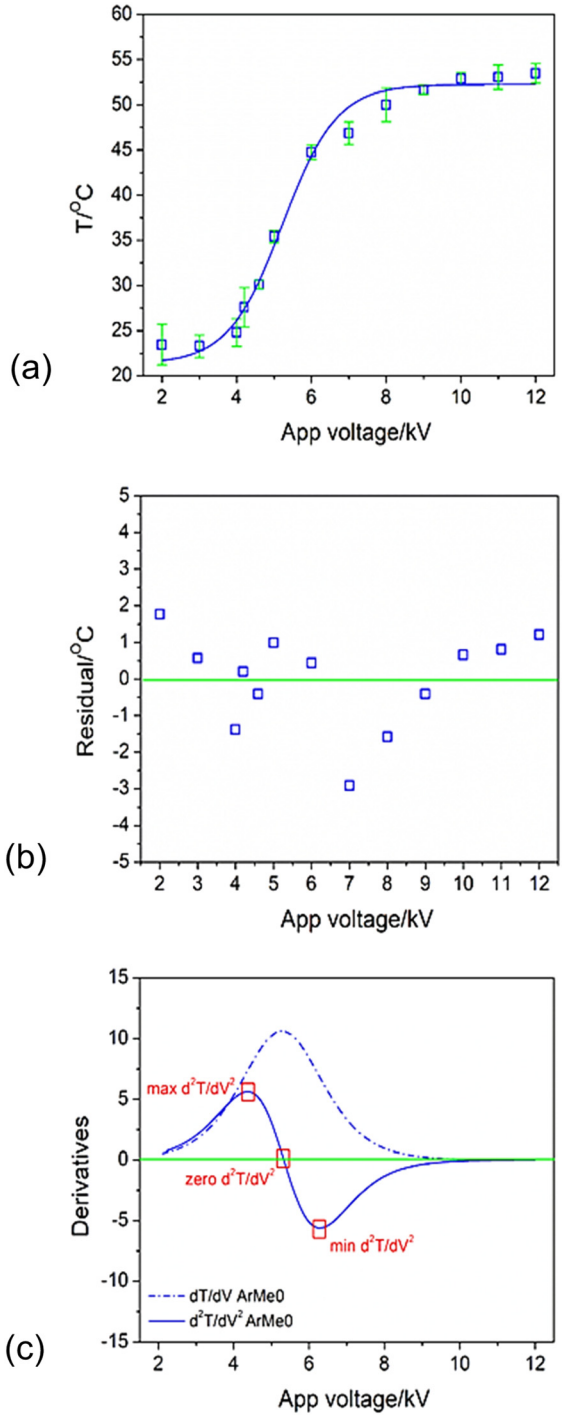


**Fig. 4** *T vs. V* data ($T(V)$) analysis using information obtained from experiments with Ar-only (ArMe0) gas. (a) $T(V)$ trend (scattered points) along with fitted curve (solid curve). (b) Corresponding residual analysis (residual calculated as the difference between observed and simulated temperature value. (c) The first and second derivatives of $T(V)$ show three points of interest (*i.e.*, maximum, zero, and minimum values of the second derivative ($T''(V)$ or $d^2T/dV^2$) indicating the point of rise, inflection, and saturation, respectively).

to the *DoseResp* model. The details of the model, values of estimated parameters, and statistics of the goodness of the fit are listed in Table 1. Values of $R^2$, *t*-value, and limits of 95% confidence interval (upper and lower limit are marked as UCL and LCL) indicate high reliability of non-linear regression. The corresponding residual distribution is shown in Fig. 4b. The order of magnitude of the fit residual is equivalent to that of the experimental measurement – more than 90% of points are within the ± 2 °C error range. The distribution of the first and second derivatives of the fitted $T(V)$ plot are shown in Fig. 4c. The points of interest, *i.e.*, points of ignition, inflection, and saturation have been identified using the $T''(V)$ plot as 4.2, 5.3, and 6.3 kV.

**Table 1** Model equation, estimated parameters, and corresponding goodness of fit parameters measured by statistical analyses

| Model | *DoseResp* (OriginPro v8.6) – a 4-parameter sigmoidal model | | | | |
|---|---|---|---|---|---|
| Equation | $y = A_1 + \frac{A_2 - A_1}{1 + 10^{(\mathrm{LOG}x_0 - x)p}}$ | | | | |
| $\chi^2$ | 1.66 | | | | |
| $R^2$ | 0.99 | | | | |
| Parameter | Value | Standard error | *t*-Value | 95% LCL | 95% UCL |
| $A_1$ | 21.32 | 1.73 | 12.31 | 17.41 | 25.24 |
| $A_2$ | 52.26 | 0.48 | 106.81 | 51.15 | 53.36 |
| $\mathrm{LOG}x_0$ | 5.22 | 0.10 | 48.02 | 4.97 | 5.47 |
| $p$ | 0.59 | 0.07 | 8.14 | 0.43 | 0.76 |

## Optical emission spectra analyses

The OES responses of pure argon (ArMe0) and argon-diluted methane (ArMe10, 10% volume basis methane in argon) are shown in Fig. 5a. The spectra resulting from carbon and/or hydrogen are attributable to the presence of methane. Characteristic peaks of argon were matched with the published data.[23] The baseline shown in Fig. 5a is the OES response when there is no plasma formed in the μR channels. The threshold point for plasma formation was the intensity of the most prominent peaks of OES (wavelength range 740–770 nm) as shown in Fig. 5b. The OES-derived data was normalized to as $\theta = I_{max}/I_0$, where $I_0$ is the maximum intensity at 751 nm at the maximum applied voltage, and $I_{max}$ is the maximum intensity at 751 nm for any specific voltage. The change in the intensity of the most prominent peak (*i.e.*, the peak at 751 nm) was tracked to estimate the ignition threshold. The distribution of $\theta$ at different applied voltages over the 4.8–5.6 kV range is shown in Fig. 5c. The baseline shown in this figure essentially is the value of $\theta$ where $I_{max}$ is the maximum intensity recorded among all data points ranging over the peak width when no electrical power was provided. In other words, the baseline demarks the maximum value of the optical emission intensity in the noisy region (marked in Fig. 5c). According to the dial markings, the minimum possible change in amplitude of voltage with the NSP generator used in this work is 0.2 kV. From the OES of plasma formed in the case of ArMe0 at different applied voltages, the threshold voltage lies between 5.2 kV and 5.4 kV.

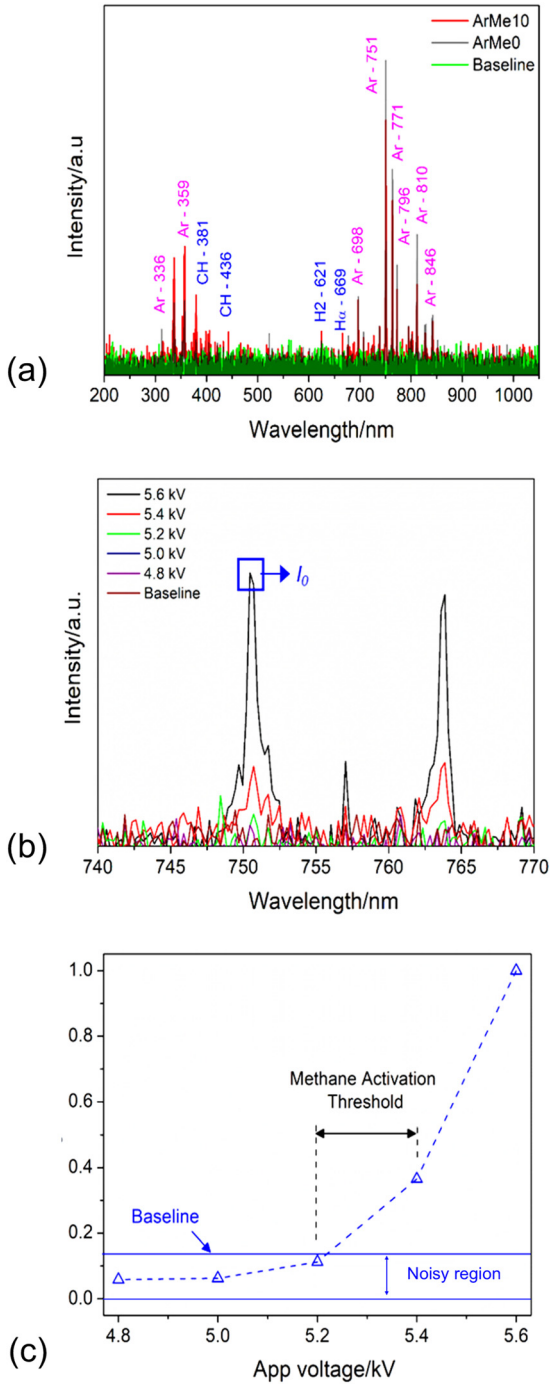


**Fig. 5** Spectral characteristics of the powered μR. (a) Optical emission spectra of pure argon and argon-methane mixture at 10 kV. (b) A closer view of the OES of pure argon obtained at a variable voltage around the threshold value (pure argon – ArMe0, 10% methane volume basis in argon – ArMe10). (c) The distribution of $\theta$ (= $I_{max}/I_0$) over a range of applied voltage for ArMe0. 200 ns wide pulses with 10 kHz frequency were used to deliver power in these experiments.

### Validation of comparative data analysis

The point of inflection (5.3 kV), among the three points of interest discussed earlier, is the closest match to the plasma formation threshold found by OES (5.2–5.4 kV) and will be the metric used to indicate plasma formation. To test this metric, the same data analysis method was applied to Ar–Me gas mixtures with different methane content. The $T(V)$ responses for methane content from 10–40% (volume basis) in argon are shown in Fig. 6a. The solid curves show the fitted $T(V)$ profiles which are a reliable fit for all the cases. The points of inflection (Fig. 6b) for 10, 20, 30, and 40% (volume basis) methane in argon occur at 5.7 kV, 7.0 kV, 7.8 kV, and 11.6 kV, respectively. Higher voltages are required to ignite mixtures having larger methane content due to the energy losses associated with vibrational excitation and dissociation of $CH_4$, which occur at lower threshold energies than electronic excitation and ionization of argon, also indicated in previous studies.[24,25] The $\theta$ for OES for these cases are shown in Fig. 6c. The methane activation thresholds estimated by OES responses are in good agreement with the corresponding points of inflection obtained from $T(V)$ analyses as illustrated in Fig. 6d. The residual plots are included in section S6 of the ESI.† The proposed data analysis technique using IR-based chip surface temperature measurement and OES extends to a range of Ar–Me gas mixtures.

### Plasma–liquid interactions

The ignition voltages produced by $T(V)$ were applied to the activation of gas-only feed systems. To test the viability of the same data analysis technique in plasma–liquid multiphase flow several organic solvents were used. The effects of operating parameters (*i.e.*, flow regime and liquid holdup) and properties of the liquid (*i.e.*, boiling point and polarity) on methane activation threshold are discussed in this section.

**Effect of liquid holdup.** The design of the μR was intended to facilitate annular gas–liquid flow. In this configuration, the liquid flows through the microreactor, wetting the side walls, leaving a central channel for gas flow. On the other hand, slug flow refers to the intermittent series of liquid slugs followed by longer gas bubbles passing through a conduit. To characterize liquid and gas flow through the μR, gas–liquid flow patterns were studied over the practical operating range of flow rates. The annular flow and slug flow regimes are shown in Fig. 7a. ArMe10 and *para*-xylene were used as the gas feed mixture and the solvent for this exercise. The slug lengths at lower gas throughputs were not homogeneous, whereas the annular flow was stable (see section S6 of the ESI†). When applying voltage, homogeneous plasma glow for slug flow was not reproducible and plasma generation was practically random.

Typical $T(V)$ for annular and slug flow under the same liquid holdup are shown in Fig. 7b. The temperature shift around the plasma formation threshold is no longer discernible for slug flow whereas a threshold can be detected for annular flow. This exercise proves the design integrity of the microreactor that was designed specifically to facilitate annular plasma–liquid multiphase flow. Design of the microreactor facilitating plasma–liquid slug flow can be found elsewhere.[26] Further experiments were conducted only in the annular flow regime.

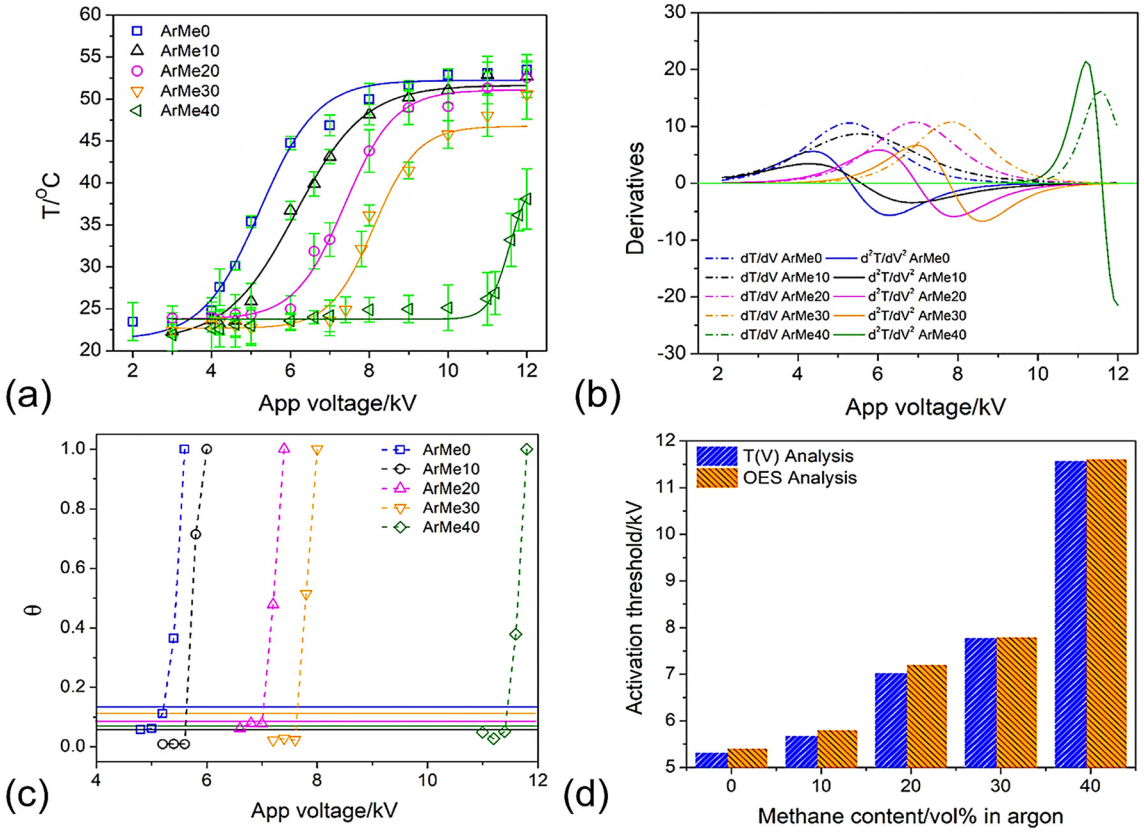


**Fig. 6** Temperature responses of the μR. (a) $T(V)$ for different compositions of ArMe feed gas mixture (scattered points) with solid curves showing regressed fit. (b) Derivative analysis (dotted curves denote the first derivative profiles; solid curves denote the second derivatives). (c) Distribution of relative peak intensity ($\theta$) over a range of applied voltage (scattered points). The dotted lines simply connect points. The horizontal solid lines are the corresponding baseline value. (d) Comparison of methane plasma ignition threshold derived from $T(V)$ and OES analyses (denoted by the upper limit of the obtained 0.2 kV range). All experiments were performed using 200 ns wide DC pulses with 10 kHz frequency.

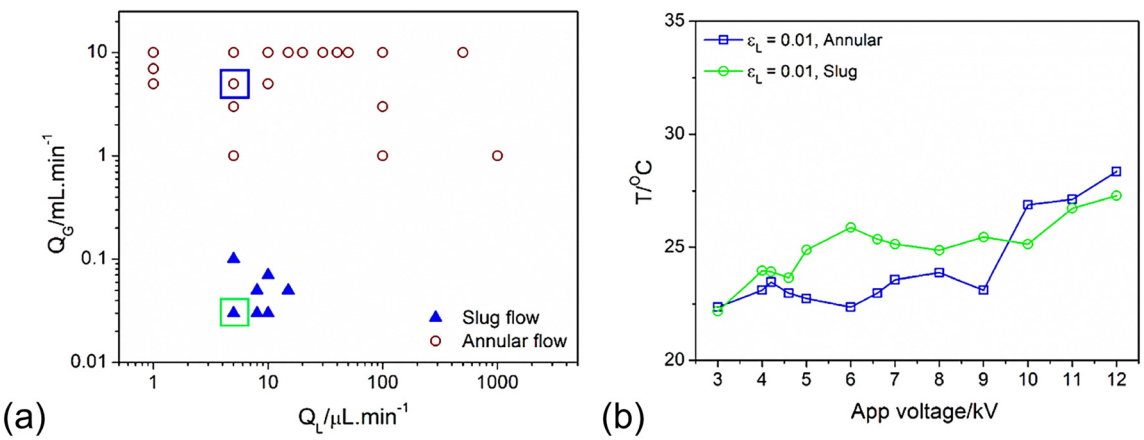


**Fig. 7** Gas–liquid flow and temperature characterization. (a) The flow regime map of microreactor μR. Marked data points were chosen for further $T(V)$ analysis. All experiments are performed using *para*-xylene as the solvent and ArMe10 as the feed gas mixture. (b) $T(V)$ response when the liquid holdup was the same (0.01), but the flow regimes were different. Experiments were conducted using DC pulses of 200 ns width at 10 kHz.

The effect of liquid holdup on methane plasma activation threshold was investigated using ArMe10 gas feed and *para*-xylene solvent over a range of $\varepsilon_L$ = 0.1–0.0001. $T(V)$ profiles, the derivative distribution, and $\theta$ obtained from corresponding OES analyses are shown in Fig. 8. The resultant methane activation thresholds are in Fig. 8d from which the reliability of the data analysis technique can be determined. The residual plots are shown in section S7 of the ESI.† The liquid holdup has an adverse effect on methane activation, *i.e.*, for the higher liquid holdup in the μR, a higher voltage is needed to sustain the plasma in the μR. Another interesting point is the gradual drop of the intensity of the most prominent OES peak (Ar peak

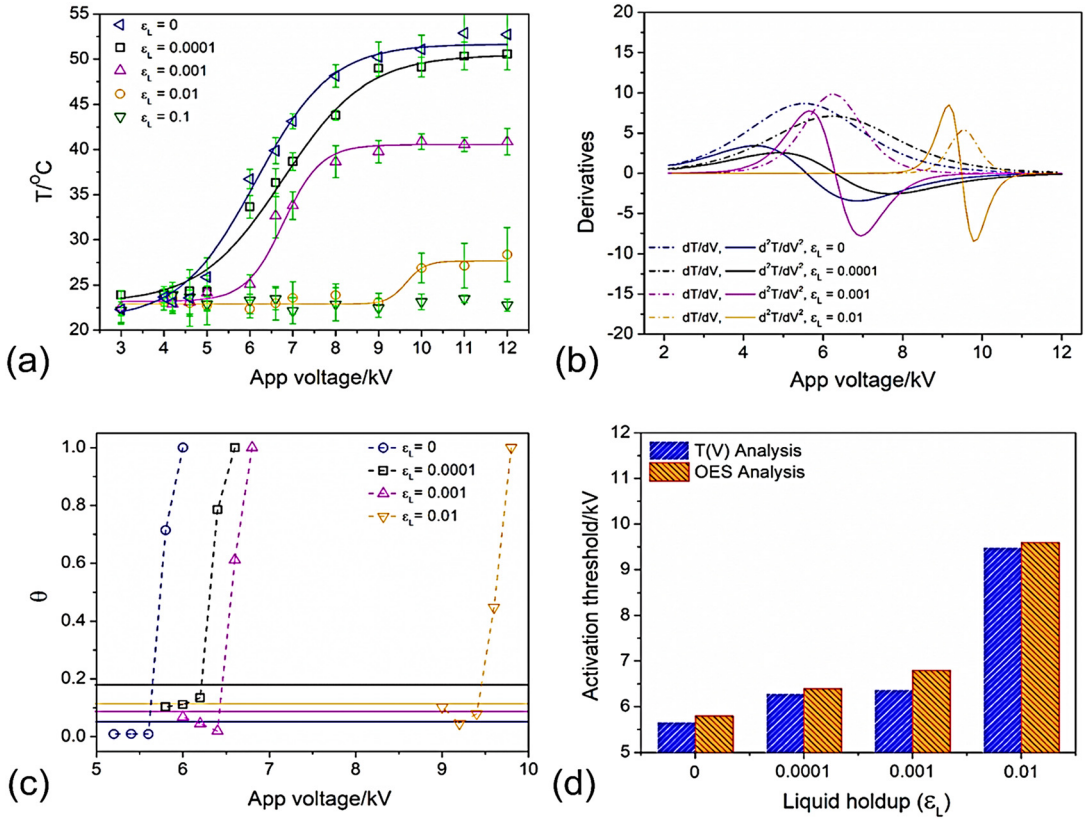


**Fig. 8** Characterization of the gas–liquid system. (a) *T*(*V*) plots for different liquid holdup of *p*-xylene for the ArMe10 feed gas mixture (scattered points). Solid curves show regressed fit. (b) Subsequent derivative analysis (dotted curves denote first derivative profiles, whereas solid curves denote the second derivatives). (c) Distribution of relative OES peak intensity ($\theta$) over a range of applied voltage (scattered points). The dotted lines simply connect points. The horizontal solid lines are the corresponding baseline values. (d) Comparison of enumerated methane plasma ignition threshold derived from *T*(*V*) and OES analyses (denoted by the upper limit of the obtained 0.2 kV range). All experiments were performed using 200 ns wide DC pulses with 10 kHz frequency.

at 751 nm) at 12 kV with increasing liquid holdup in the system. This not only illustrates the non-equilibria of the plasma phase but also aids our statement on liquid holdup having an adverse effect on plasma ignition. More intense plasma resulted in higher top surface temperature. For high liquid holdup ($\varepsilon_L \sim$ 0.1 and above), plasma formation was not observed over the range of voltage tested, 3–12 kV. Low liquid holdup ($\varepsilon_L \sim$ 0.0001 and below) resulted in frequent drying up of the liquid films. Further experiments were performed using a liquid holdup of 0.001 to ensure uninterrupted data acquisition.

**Effect of dielectric constant and boiling point of liquid.** Organic liquids were chosen to enable the evaluation of the effect of specific liquid properties on plasma formation. For example, benzene and alkylbenzenes like toluene, ethylbenzene, and *p*-xylene were selected to understand the effect of boiling point as their dielectric constants are similar (~2.3–2.5 at NTP). Acetonitrile and 1,2-dichloroethane (DCE) were chosen as their boiling points are similar to benzene (80 ± 2 °C at atmospheric pressure) while their dielectric constants are different (ranging from 2–37). The boiling points and

**Table 2** Organic liquids used in this study

| Solvent[a] | $D_c$[b] | bp/°C[d] | $T_{12kV}$/°C[c] | $I_{0,12kV}$[e] | $V_{th,T}$/kV[f] | $V_{th,O}$/kV[g] |
|---|---|---|---|---|---|---|
| Benzene | 2.3 | 80 | 36.1 | 340 | 6.4 | 6.4–6.6 |
| Toluene | 2.4 | 110 | 40.2 | 430 | 6.3 | 6.2–6.4 |
| Ethylbenzene | 2.5 | 136 | 40.5 | 450 | 6.3 | 6.2–6.4 |
| *p*-Xylene | 2.3 | 140 | 40.7 | 450 | 6.3 | 6.4–6.6 |
| Acetonitrile | 37.5 | 82 | 42.6 | 490 | 5.8 | 5.8–6.0 |
| 1,2-DCE | 10.4 | 78 | 39.8 | 390 | 6.0 | 5.8–6.0 |
| Acetone | 20.7 | 56 | 27.5 | 20 | Na | Na |

[a] >99% (weight basis) pure assay, used as procured. [b] Dielectric constant at NTP. [c] Measured temperature at 12 kV applied voltage (Abs. error = ±2 °C). [d] Boiling point at atmospheric pressure. [e] Intensity of the peak at 751 nm at 12 kV applied voltage (Abs error ±20%), in arb. units. [f] $V_{th,T}$ – threshold voltage calculated from *T*(*V*) analysis. [g] $V_{th,O}$ – threshold voltage calculated from OES analysis.

 

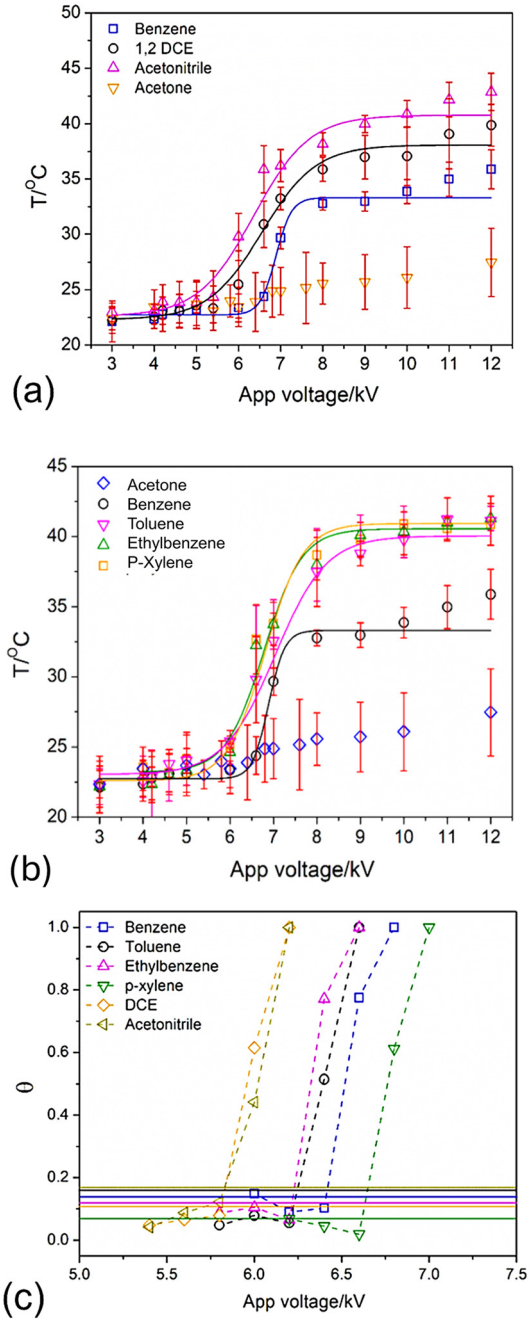


**Fig. 9** Temperature characteristics for different gas–liquid systems. (a) $T(V)$ responses of acetone and different organic liquids with similar boiling points but different dielectric constants. (b) $T(V)$ responses of acetone and different organic liquids with similar dielectric constant but different boiling points, (scattered points show observed data, solid curves show regressed fit). (c) Distribution of relative OES peak intensity ($\theta$) over a range of applied voltage (scattered points). The dotted lines simply connect points. Coloured horizontal solid lines show corresponding baseline value.

dielectric constants of these liquids are listed in Table 2. 10% methane (volume basis) diluted in argon (ArMe10) was used as the gas feed. The NSP was operated with variable voltage, 10 kHz pulse repetition frequency, and 200 ns pulse width. The experiments were performed around a liquid holdup of 0.001.

To quantify the effect of the solvent polarity on the methane activation voltage threshold, the data analysis technique was employed for benzene, DCE, acetone, and acetonitrile. The resulting $T(V)$ profiles are shown in Fig. 9a. To quantify the effect of boiling point on the liquid, $T(V)$ responses of benzene along with the other three alkylbenzenes with similar polarizability are shown in Fig. 9b. Corresponding OES-derived $\theta$ distributions are shown in Fig. 9c. The $T$-residual plots and corresponding derivative distributions are shown in section S7 of the ESI.† Low dielectric constant and low boiling point of liquid have a negative impact on plasma generation.

With the increase in methane fraction in argon, organic vapor in the gas phase tends to raise the threshold voltage for plasma activation. Organic solvents are even larger molecules than methane, having more vibrational modes and more channels for electron impact dissociation and ionization. The electron energy loss to vibrational, electron excitation, and ionization are expected to be proportionately larger. The methane activation threshold for highly polar solvents like acetonitrile is lower than that of non-polar solvents like benzene, likely due to their lower vapor pressure (once in the gas phase, more polar molecules are expected to be more reactive with electrons than non-polar molecules). Homogeneous plasma glow was not observed when using acetone over the range of applied voltage while acetone films tended to dry up when high voltage was applied across the μR chip. This change in flow from an annular to a mist flow produces more avenues for electron energy loss and so a decrease in methane activation (requiring higher voltages).

As shown in Table 2, the measured temperature at 12 kV applied voltage for plasma–liquid systems (denoted by $T_{12kV}$) and the intensity of the most prominent peak (at 751 nm) at 12 kV applied voltage (denoted by $I_{0,12kV}$) follow an interesting pattern. Lower-intensity plasma resulted in a smaller OES peak and lower surface temperature. $T_{12kV}$ and $I_{0,12kV}$ are both absolute values that depend upon numerous factors and can alter significantly from system to system, especially OES intensity. That's why the absolute error in $I_{0,12kV}$ is significantly large. Yet, the trend corroborates that the lower boiling point and lower dielectric constant of the liquid in the system hinder plasma ignition. When plasma is ignited, higher polarity of the liquid phase results in higher intensity plasma. Acetone has a lower boiling point and higher polarity than benzene. The $T(V)$ analysis indicates that the plasma ignition threshold is more sensitive to boiling point (and so vapor pressure) than polarity. The phase change of the whole or a fraction of the liquid film (can also be referred to as thinning of the liquid film) due to the presence of ArMe plasma in micro-confinements needs to be investigated in detail. The methane plasma ignition threshold obtained from $T(V)$ analyses ($V_{th,T}$) is compared with that obtained from OES analyses ($V_{th,O}$) in Table 2, showing overall good agreement for this range of operating conditions.

## Conclusions

The interaction of atmospheric pressure dielectric barrier discharge plasmas sustained in argon-diluted methane in a microreactor was investigated with and without a co-flow of organic solvents. The in-house designed borosilicate/silicon DBD microreactor chip (μR) had a 500 μm × 500 μm square cross-section and ~1 m length. The consequences of methane fraction and liquid co-flow on plasma ignition voltage were investigated. Operating conditions included varying applied voltage, fluid flow pattern, liquid holdup, and liquid properties. The co-flow organic solvents were benzene, toluene, *p*-xylene, ethylbenzene, acetonitrile, acetone, and 1,2-dichloroethane. The data analysis technique combined optical emission spectroscopy and chip surface temperature monitoring to estimate the methane activation threshold voltage. The investigation intended to enable the detection of plasma activation in systems that may not have optical access (the definitive measure of plasma formation) while being able to measure chip temperature *vs.* voltage $T(V)$. The point of inflection of the $T(V)$ profile was correlated with the OES-derived plasma formation (and thereby methane activation) threshold for the range of plasma–liquid interactions investigated. This method can be used to narrow the operating range of electrical and process parameters to achieve stable plasma glow discharges in plasma–liquid systems operating in micro confinements. Doing so potentially enables a quantitative study of reaction kinetics involving methane plasmas in microreactors.

## Data availability

The data supporting this article have been included as part of the ESI.†

## Author contributions

SD, MM, and RLH conceived the idea; MM and RLH designed the reactor; SD developed the methodology, conducted the experiments, analyzed the data, created the graphics, and drafted the manuscript; MJK and RLH reviewed the manuscript; RLH oversaw the project. All authors have approved the final version of the manuscript.

## Conflicts of interest

There are no conflicts to declare.

## Acknowledgements

The authors acknowledge the National Science Foundation's Environmental Convergence Opportunities in Chemical, Bioengineering, Environmental, and Transport Systems (award numbers ECO-CBET 2032604 and 2032664) of the National Science Foundation (NSF) of the United States for funding; and the nanofabrication facilities (the Cornell NanoScale Facility (CNF), Cornell University and Quattrone Nanofabrication Facility (QNF), Singh Center for Nanotechnology, University of Pennsylvania) for their support.

## References

1 H. Puliyalil, D. L. Jurković, V. D. B. C. Dasireddy and B. Likozar, *RSC Adv.*, 2018, **8**, 27481–27508.
2 U.S. Energy Information Administration (EIA) report on "U.S. Energy Information Administration - EIA - Independent Statistics and Analysis." (accessed on May 22, 2024).
3 B. Ruscic, *J. Phys. Chem. A*, 2015, **119**, 7810–7837.
4 M. Wullenkord, K. H. Funken, C. Sattler and R. Pitz-Paal, *18th World Hydrogen Energy Conference 2010*, Essen, May, 2010.
5 Y. Uytdenhouwen, K. M. Bal, E. C. Neyts, V. Meynen, P. Cool and A. Bogaerts, *Chem. Eng. J.*, 2021, **405**, 126630.
6 Y. X. Zeng, L. Wang, C. F. Wu, J. Q. Wang, B. X. Shen and X. Tu, *Appl. Catal., B*, 2018, **224**, 469–478.
7 P. Chawdhury, Y. Wang, D. Ray, S. Mathieu, N. Wang, J. Harding, F. Bin, X. Tu and C. Subrahmanyam, *Appl. Catal., B*, 2021, **284**, 119735.
8 C. Xu and X. Tu, *J. Energy Chem.*, 2013, **22**, 420–425.
9 L. Wang, Y. Yi, C. Wu, H. Guo and X. Tu, *Angew. Chem., Int. Ed.*, 2017, **56**, 13679–13683.
10 Y. Yi, X. Wang, A. Jafarzadeh, L. Wang, P. Liu, B. He, J. Yan, R. Zhang, H. Zhang, X. Liu, H. Guo, E. C. Neyts and A. Bogaerts, *ACS Catal.*, 2021, **11**, 1765–1773.
11 Y. Yi, S. Li, Z. Cui, Y. Hao, Y. Zhang, L. Wang, P. Liu, X. Tu, X. Xu, H. Guo and A. Bogaerts, *Appl. Catal., B*, 2018, **296**, 120384.
12 A. Bogaerts, G. Centi, V. Hessel and E. Rebrov, *Catal. Today*, 2023, **420**, 114180.
13 L. Patinglag, D. Sawtell, A. Iles, L. M. Melling and K. J. Shaw, *Plasma Chem. Plasma Process.*, 2019, **39**, 561–575.
14 C. Ishii, S. Stauss, K. Kuribara, K. Urabe, T. Sasaki and K. Terashima, *Diamond Relat. Mater.*, 2015, **59**, 40–46.
15 Y. Yamanishi, S. Sameshima, H. Kuriki, S. Sakuma and F. Arai, *17th International Conference on Solid-State Sensors, Actuators and Microsystems*, Barcelona, June, 2013.
16 J. Wengler, S. Ognier, M. Zhang, E. Levernier, C. Guyon, C. Ollivier, L. Fensterbank and M. Tatoulian, *React. Chem. Eng.*, 2018, **3**, 930–941.
17 D. Huh, C. H. Kuo, J. B. Grotberg and S. Takayama, *New J. Phys.*, 2009, **11**, 075034.
18 T. Cubaud and C. M. Ho, *Phys. Fluids*, 2004, **16**, 4575–4585.
19 M. T. Kreutzer, F. Kapteijn, J. A. Moulijn and J. J. Heiszwolf, *Chem. Eng. Sci.*, 2005, **60**, 5895–5916.
20 M. Suo and P. Griffith, *J. Basic Eng.*, 1964, **86**, 576–582.
21 N. Brauner and D. M. Maron, *Int. Commun. Heat Mass Transfe*, 1992, **19**, 29–39.
22 Origin Lab documentation (accessed on May 22, 2024).
23 A. Chingsungnoen, J. I. B. Wilson, V. Amornkitbamrung, C. Thomas and T. Burinprakhon, *Plasma Sources Sci. Technol.*, 2007, **16**, 434–440.
24 M. V. Pachuilo, F. Stefani, R. D. Bengtson, Dipti, R. Srivastava and L. L. Raja, *IEEE Trans. Plasma Sci.*, 2017, **45**, 1776–1787.
25 M. M. Moshrefi and F. Rashidi, *J. Nat. Gas Sci. Eng.*, 2014, **16**, 85–89.
26 P. Dedieu, G. Morand, K. Loubière, S. Ognier and M. Tatoulian, *Lab Chip*, 2024, **24**, 3898–3908.

 